Supporting Information

In-situ gelation regulating micro-electric fields to induced Li deposition in quasi-solid-state lithium metal batteries

Qiyu Wang [a], Xiangqun Xu [a], Bo Hong [a,b] *, Maohui Bai [a], Jie Li [a], Zhian Zhang [a], Yanqing Lai [a,b] *

[a] School of Metallurgy and Environment, Central South University, Changsha 410083, PR China.

[b] Engineering Research Centre of Advanced Battery Materials, The Ministry of Education, Changsha 410083, Hunan, China

*Corresponding author.

E-mail address: bop_hong@163.com (B. Hong); laiyanqing@csu.edu.cn (Y. Lai).

Supporting Information Contains:

S1. Calculation of ionic conductivity

The ionic conductivity (σ) can be calculated using the following equation:

$$\sigma = \frac{I}{R_b A}$$

where I stands for the film thickness, R_b represents the bulk resistance, and A represents the area.

S2. Calculation of Li^+ transference numbers

The Li^+ transference numbers (t_{Li+}) were measured by DC polarization/AC impedance in symmetric Li/GPEs/Li cells. The t_{Li+} value can be calculated using the following equation:

$$t_{Li}^{+} = \frac{I_{ss}(\Delta V - I_0 R_0}{I_0(\Delta V - I_{ss} R_{ss})}$$

where ΔV is the polarization voltage applied (10 mV), I_0 and R_0 represent the initial current and interfacial resistance respectively, and I_{SS} and R_{SS} are the steady-state current and interfacial resistance after polarization for 10000 s, respectively.

S3. Calculation of activation energy

Activation energy (E_a) was used to demonstrate the difficulty level of Li-ion transference. The behavior of σ and E_a mainly obeys the Arrhenius equation:

$$\sigma = \sigma_0 exp(-E_a/RT)$$

S4. Choice on different Li^+ adsorption sites

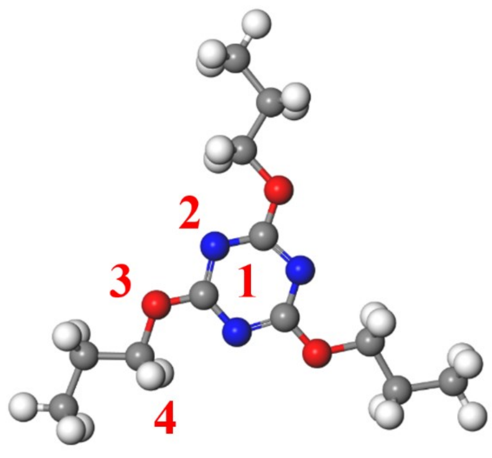

Figure S1. Choice on different Li^+ adsorption sites

S5. Crystal models for calculating the binding energy

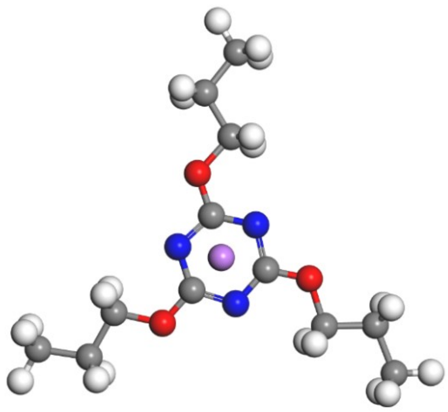

E_b=-1.37 eV

Figure S2. Crystal models for calculating the binding energy of a Li^+ adsorbed on position 1

S6. Corresponding charge density difference

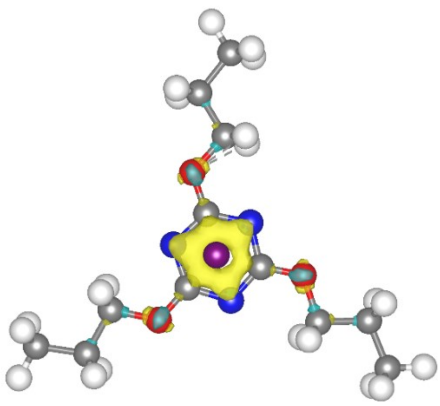

Figure S3. corresponding charge density difference (gray, blue, red, and purple balls represent carbon atoms, nitrogen atoms, oxygen atoms and Li atoms, respectively; yellow and light blue areas represent positive and negative charge differences, respectively)

S7. Room temperature storage experiment

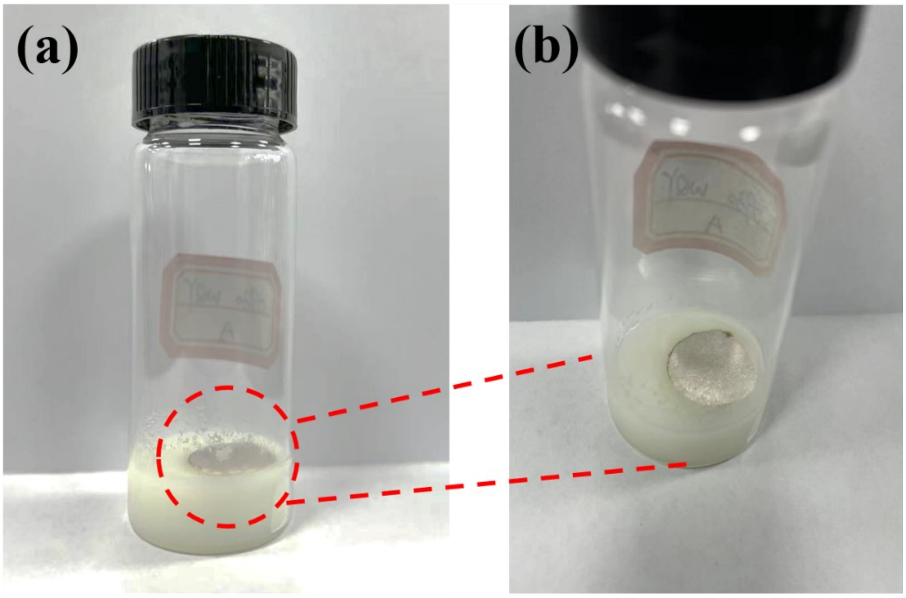

Figure S4. Room temperature storage experiment

S8. TGA analysis of commercial separator

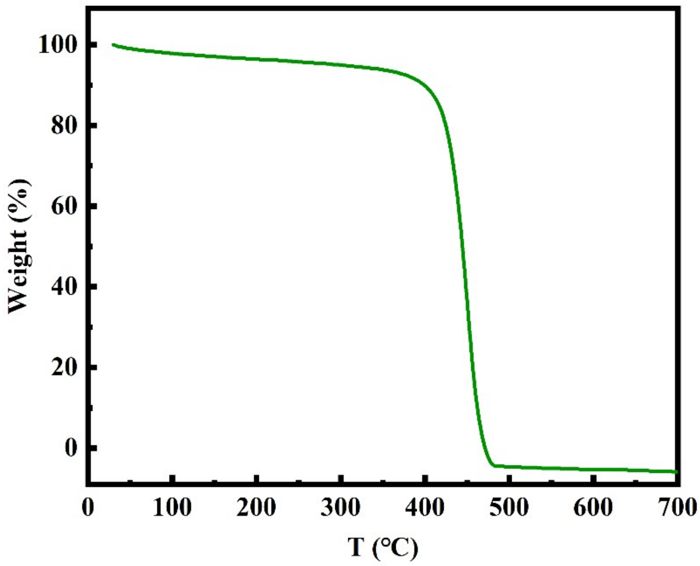

Figure S5. TGA analysis of commercial separator.

S9. EIS of a SS|GPE 1%|SS symmetrical cell with the elevation of temperature

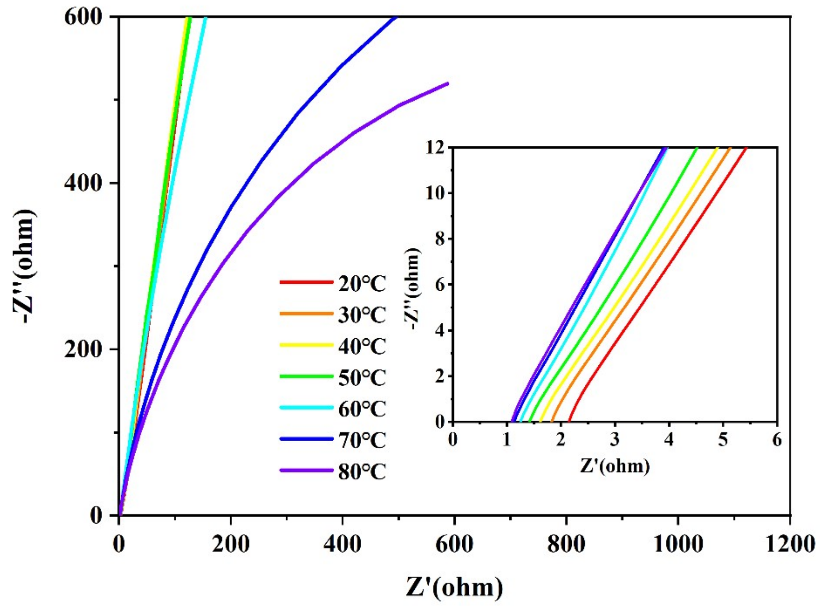

Figure S6. EIS of a SS|GPE 1%|SS cell with the elevation of temperature

S10. EIS of a SS|GPE 2%|SS symmetrical cell with the elevation of temperature

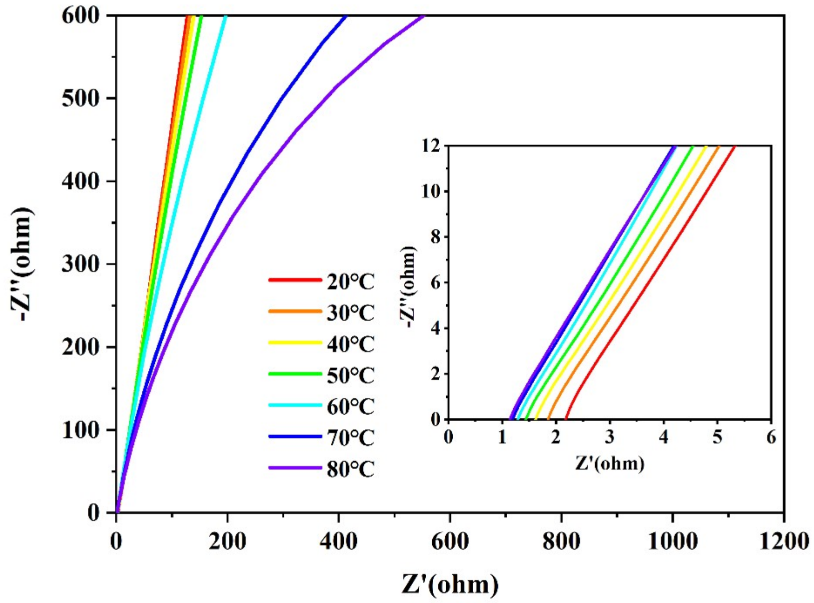

Figure S7. EIS of a SS|GPE 2%|SS cell with the elevation of temperature

S11. EIS of a SS|GPE 5%|SS symmetrical cell with the elevation of temperature

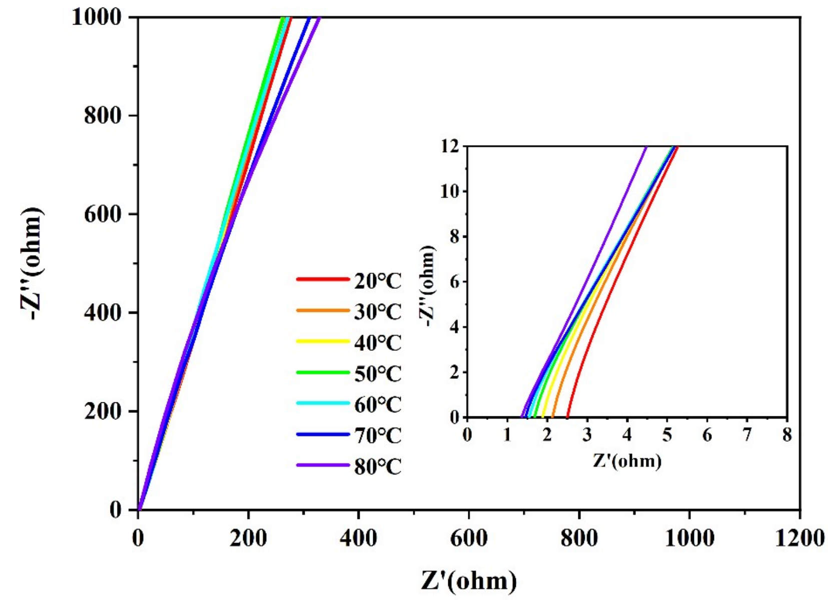

Figure S8. EIS of a SS|GPE 5%|SS cell with the elevation of temperature

S12. Charge/discharge voltage curves of $LiFePO_4$|GPE 1%|Li

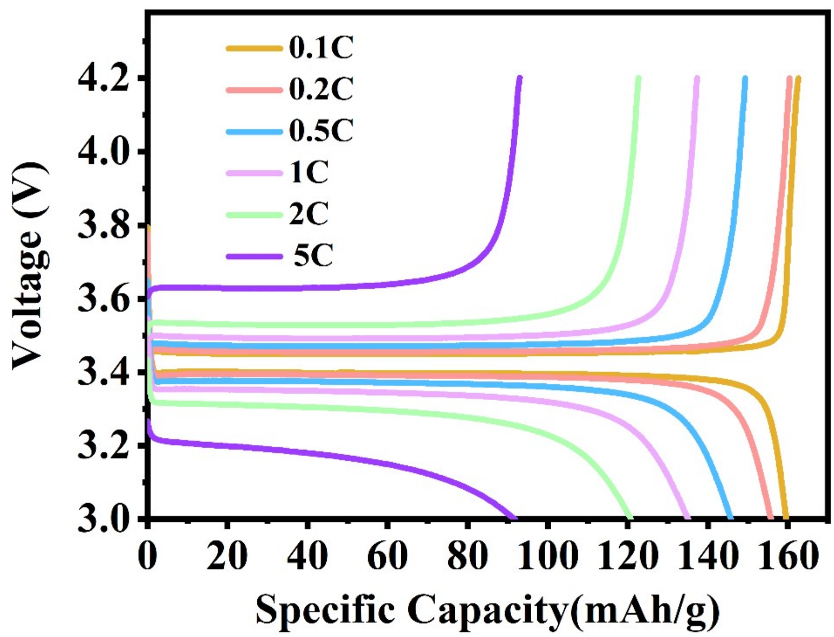

Figure S9. Charge/discharge voltage curves of $LiFePO_4$|GPE 1%|Li

S13. Charge/discharge voltage curves of $LiFePO_4$|GPE 5%|Li

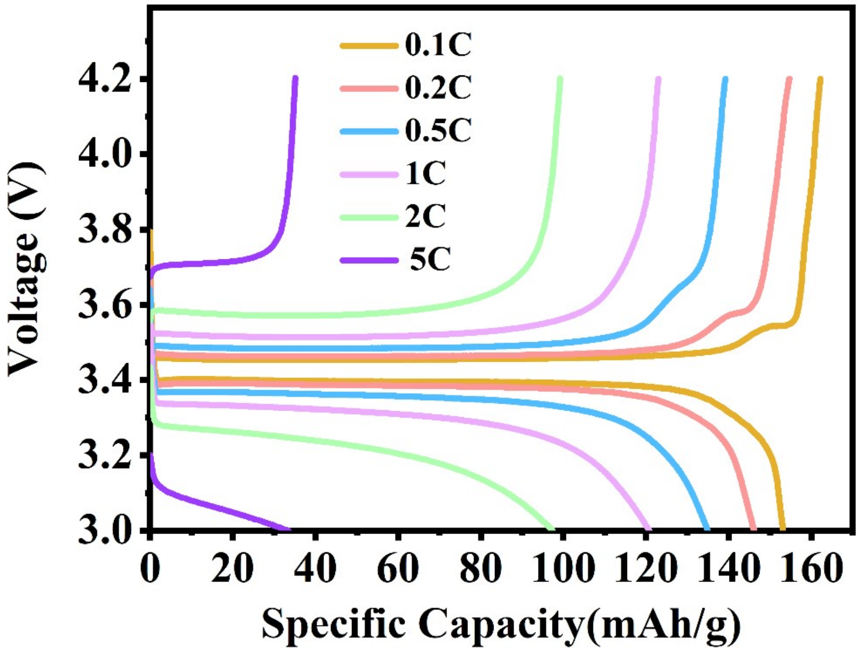

Figure S10. Charge/discharge voltage curves of $LiFePO_4$|GPE 5%|Li

S14. Cyclic voltammograms and rate capability of LiFePO4|LE|Li cell

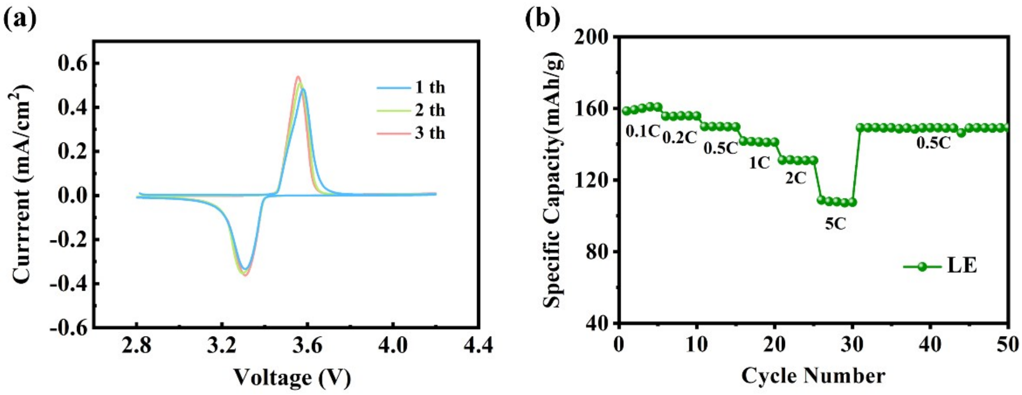

Figure S11. Cyclic voltammograms (a) and rate capability(b) of $LiFePO_4$|LE|Li cell

S15. Calculated DLi^{+} for LFP cathodes in $LiFePO_4$|LE|Li cell

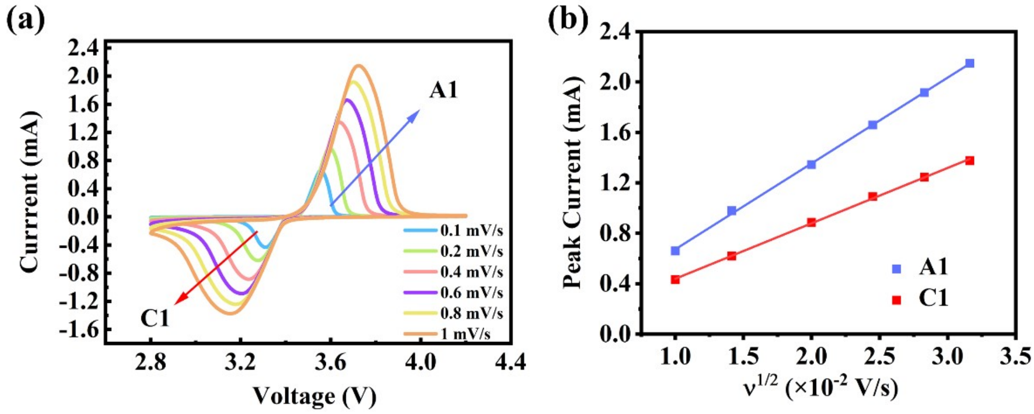

Figure S12. (a) The CV curve of $LiFePO_4$|GPE|Li at various sweep rates. (b) The slopes of redox peaks current of $LiFePO_4$|GPE|Li from CVs vs. a square root function of sweep rates.

S16. XPS analysis of lithium metal anode in GPE system after 10 cycles

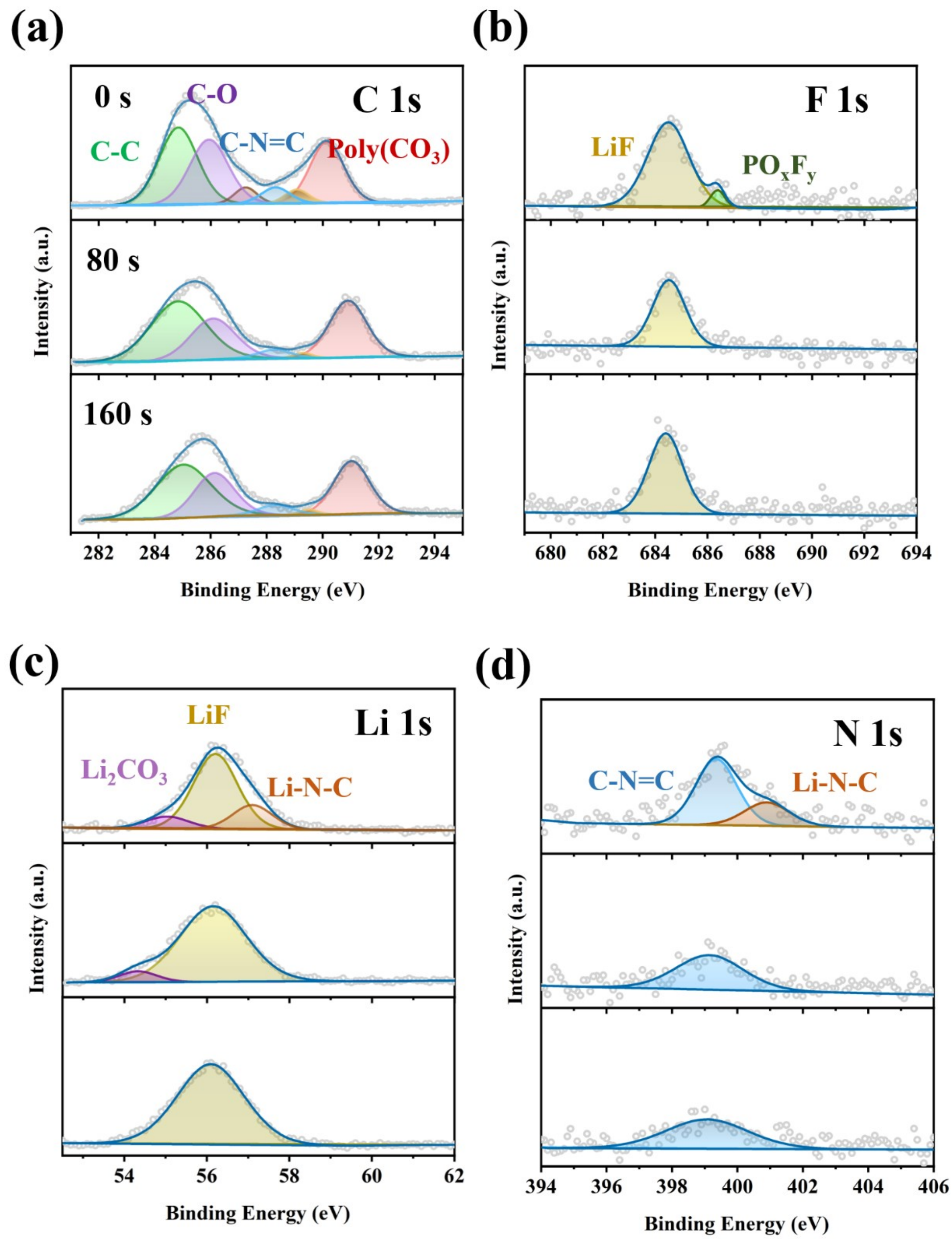

Figure S13. XPS spectra of C 1s (a), F 1s (b), Li 1s (c) and N (d) for lithium metal retrieved from GPE in 10 cycles.

S17. XPS analysis of lithium metal anode in LE system after 10 cycles

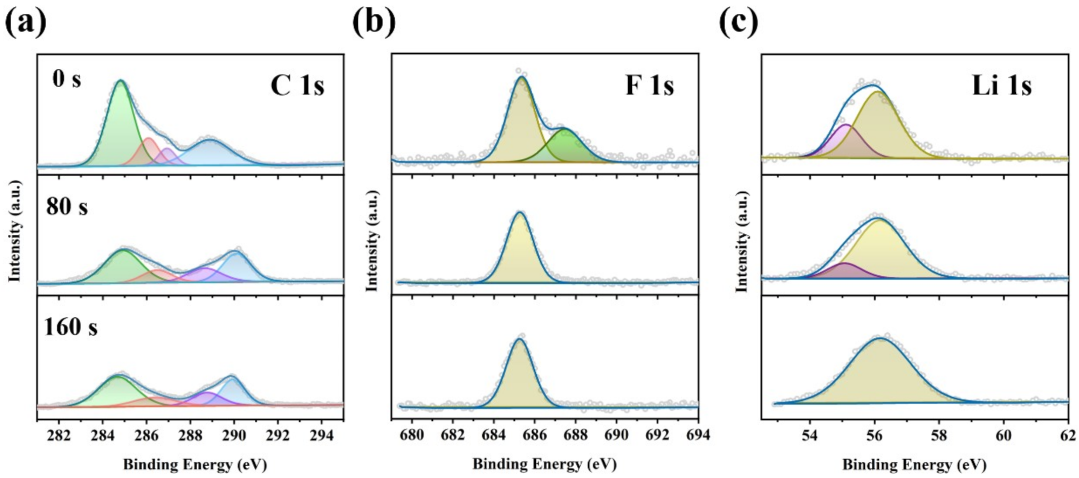

Figure S14. XPS spectra of C 1s (a), F 1s (b) and Li 1s (c) for lithium metal retrieved from LE in 10 cycles.

S18. Atomic ratios of SEI formed in the LE

Table S1 Atomic ratios of SEI formed in the LE

Etch Time (s)	Li (atomic %)	C (atomic %)	F (atomic %)
0	42.476	50.842	6.682
80	65.376	19.804	14.820
160	71.956	16.364	11.680

S19. Atomic ratios of SEI formed in the GPE

Table S2 Atomic ratios of SEI formed in the GPE

Etch Time (s)	Li (atomic %)	C (atomic %)	N (atomic %)	F (atomic %)
0	32.022	62.840	2.118	3.020
80	47.955	46.469	1.680	3.896
160	54.141	40.521	1.438	3.900

S20. Schematic illustration of Li^+ transporting process in SEI on Li anode

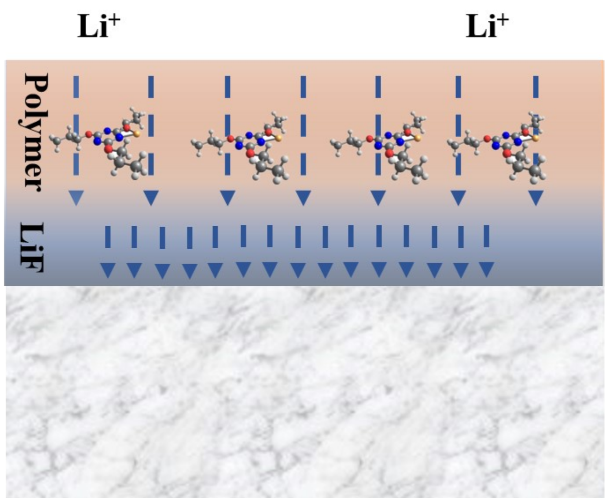

Figure S15. Schematic illustration of Li+ transporting process in SEI on Li anode

S21. Electrochemical performances of gel electrolytes reported in the literature

Table S3. Electrochemical performances of gel electrolytes reported in the literature

GPE ingredients	Room temperature ionic conductivity/ (mS/cm)	Preparation method	Cell(cycles)capacity retention/C-rate	Ref
Poly (diethylene glycol carbonate)	0.16	In situ	LFP/Li(100th)95%/0.2C	1
PVDF GPE with BN additive	0.81	Ex situ	LFP/Li(300th)88%/1C	2
Polymerized poly (tetrahydrofuran)	0.23	In situ	LFP/Li(100th)91.3%/0.1C	3
Ultraviolet solidified gel electrolyte	1	In situ	LFP/Li(200th)77.6%/1C	4
PE supported GPE	0.45	Ex situ	LCO/Li(300th)62.7%/0.2C	5
PMMA/PVDF hybrid polymer	-	Ex situ	NCA/Li(200th)86.1%/1C	6
A dual-salt cross-linked network	0.56	In situ	LFP/Li(300th)87.9%/0.5C	7
PEGDA GPE with CA additive	8.81	In situ	LCO/Li(100th)87%/0.5C	8
A borate-rich 3D network	0.84	In situ	LFP/Li(400th)89.7%/0.5C	9
A hybrid polymer network	7.6	In situ	LFP/Li(500th)90%/0.5C	10
polymer with triazine centres	7.93	In situ	LFP/Li(700th)80.6%/1C	This work

[1] Liu X, Ding G, Zhou X, et al. An interpenetrating network poly (diethylene glycol carbonate)-based polymer electrolyte for solid state lithium batteries[J]. Journal of Materials Chemistry A, 2017, 5(22): 11124-11130.

[2] Shim J, Kim H J, Kim B G, et al. 2D boron nitride nanoflakes as a multifunctional

additive in gel polymer electrolytes for safe, long cycle life and high rate lithium metal batteries[J]. Energy & Environmental Science, 2017, 10(9): 1911-1916.

[3] Huang S, Cui Z, Qiao L, et al. An in-situ polymerized solid polymer electrolyte enables excellent interfacial compatibility in lithium batteries[J]. Electrochimica Acta, 2019, 299: 820-827.

[4] Zhang S Z, Xia X H, Xie D, et al. Facile interfacial modification via in-situ ultraviolet solidified gel polymer electrolyte for high-performance solid-state lithium ion batteries[J]. Journal of Power Sources, 2019, 409: 31-37.

[5] Wang Y, Fu L, Shi L, et al. Gel polymer electrolyte with high Li^+ transference number enhancing the cycling stability of lithium anodes[J]. ACS applied materials & interfaces, 2019, 11(5): 5168-5175.

[6] Zhou Z, Feng Y, Wang J, et al. A robust, highly stretchable ion-conducive skin for stable lithium metal batteries[J]. Chemical Engineering Journal, 2020, 396: 125254.

[7] Fan W, Li N W, Zhang X, et al. A dual-salt gel polymer electrolyte with 3D cross-linked polymer network for dendrite-free lithium metal batteries[J]. Advanced Science, 2018, 5(9): 1800559.

[8] Liu M, Wang Y, Li M, et al. A new composite gel polymer electrolyte based on matrix of PEGDA with high ionic conductivity for lithium-ion batteries[J]. Electrochimica Acta, 2020, 354: 136622.

[9] Dai K, Ma C, Feng Y, et al. A borate-rich, cross-linked gel polymer electrolyte with near-single ion conduction for lithium metal batteries[J]. Journal of Materials Chemistry A, 2019, 7(31): 18547-18557.

[10] Wang Q, Xu X, Hong B, et al. Molecular engineering of a gel polymer electrolyte via in-situ polymerization for high performance lithium metal batteries[J]. Chemical Engineering Journal, 2021, 131331.